Development and Verification of Reduced-Order Model for Diesel Spray Penetration and Spreading during Wall Impingement

Author, co-author list (Do NOT enter this information. It will be pulled from participant tab in MyTechZone)

Affiliation (Do NOT enter this information. It will be pulled from participant tab in MyTechZone)

Abstract

The mixing of a diesel spray with in-cylinder gases is driven by both turbulent mixing during the free-jet penetration phase and by mixing during the jet's impingement on surfaces such as the piston bowl. Current reduced order models, and many experiments, focus solely on the free-jet penetration phase, although jet-wall interaction occurs during a significant portion of the duration of a fuel injection in both small-bore and large-bore engines. A control volume-based model for the spreading of an impinging spray along a flat wall is presented as a first step towards capturing key jet processes during the impingement phase of fuel injection. Schlieren measurements of impinging gaseous jets are used to evaluate the model. The impinging jet model is then coupled with the free jet model of Musculus and Kattke to compare global entrainment effects at various diesel conditions, providing a means for evaluating the effects of combustion parameters on entrainment with more realistic engine geometries.

Introduction

The reduction of pollutant emissions in diesel engines is a growing initiative in automotive design: recent regulations limit the emission of NO_x and soot and set minimums for efficiency [1] [2]. In order to meet these standards, automotive manufacturers will require a greater understanding of the fuel injection and combustion processes, in which the fuel spray's impingement onto engine hardware plays a large role.

Characterization of diesel impingement phenomena

Much of the work on fuel spray characterization, using either liquid sprays or gaseous jets, has been done for free sprays. However, spray impingement with piston features affects combustion through mixing and heat transfer phenomena, and its overall impact on engine performance is not well understood [3]. In order to isolate phenomena associated with impingement from effects relating to spray-spray interaction or other complexities encountered in an engine, plane wall jets are often studied [4]. Pickett and Lopez [4], for example, studied combustion outcomes from reacting diesel sprays in a constant-volume combustion vessel. They note that the introduction of a wall can eliminate soot when imposed on a sooting free spray, suggesting that increased mixing with ambient air or thermal effects cooling the spray lead to desirable outcomes.

Li *et al.* [3] investigated the effects of injection pressure and wall distance on the combustion and spray characteristics of an impinging diesel jet. At lower injection pressures, the authors note that the interaction between the spray and the wall lead to higher unburned hydrocarbon emissions, greater soot formation, and a lower heat release, due to increased heat transfer to the wall and wetting effects. Soot formation is mitigated with increasing injection pressure. The free spray is burned more completely than the corresponding impinging spray. The authors suggest that an optimal condition exists when combustion begins just before impingement.

Imaging the liquid and vapor phases in non-reacting, vaporizing impinging sprays at two injection pressures and nozzle sizes, Zhang *et al.* [5] found that the empirical wall jet correlation of Glauert [6] under-predicted the radial penetration of the two-phase diesel spray, but did so to a lesser extent for sprays with an ultra-small orifice ($d_o = 0.08$ mm). The researchers also found that higher injection pressures improved the mixing characteristics near the wall after EOI, and that smaller nozzle orifices lead to less fuel accumulating in a film along the wall. Wang *et al.* [7] performed similar experiments at reacting conditions, finding lower soot resulting from smaller nozzle orifices. This is attributed to the decreased wall-wetting explained in [5].

Studies have also investigated the impact that bowl geometry has on mixing and reaction outcomes. Zhang and Nishida [8] investigated mixing effects of multiple-injection fuel delivery strategies with a model piston bowl. Studying non-reacting conditions, the authors produced detailed measurements of liquid- and vapor-phase fuel in realistic geometries. Eismark's experiment [9] provided a direct, side-by-side comparison of free and impinging reacting sprays, with one half of a spray impinging on a curved surface and the other continuing past.

These many studies have shown that the presence of a wall impacts important combustion outcomes and suggest that these outcomes are driven, at least in part, by the way wall interaction impacts fuel-air mixing. Thus, a model that captures these mixing characteristics, and how they are impacted by injection parameters, could help in understanding the ways in which wall impingement can be optimized for lower emissions.

Use of gaseous jets to study diesel sprays

One way diesel injection is studied is through simulation with gas jets, which behave similarly to diesel sprays [10] and allow for more optically-accessible experiments. In particular, the liquid droplets and wide temperature variations in reacting diesel sprays hinder laser diagnostics like laser-induced fluorescence (LIF) and particle image velocimetry (PIV) [11]. Working with gas jets, researchers can determine the ways

in which fuel injections in a sequence will interact with each other and the surrounding engine geometry: the scaling relations fundamental to the study of fluid mechanics allow the penetration and mixing of a gas jet to be related to that of a diesel spray.

Bruneaux, Causse and Omrane [11] used high-pressure gas jets to simulate diesel sprays, matching ambient density and mass flow rate between their experiment and relevant diesel conditions. Their PIV and LIF measurements gave detailed spray velocity and concentration profiles that would not have been attainable studying in-engine diesel sprays. Abani and Ghandhi [12] measured the effects of varying the injection rate profile on the penetration rate of helium jets injected into atmospheric conditions. To study fluids effects of multiple-injection injection schedules, Borz *et al.* [13] compared the penetration rates of free gas jets to those injected into their wakes.

Computational simulations of gas jets are used to study diesel sprays, as well: Eismark *et al.* [14] studied the role turbulence plays in mixing with a large-eddy simulation of a gas jet that matched the properties of the impinging diesel spray investigated experimentally in [9].

Impinging gas jets

Given the ability of gaseous jets to exhibit phenomena observed in diesel sprays, a review of impinging gas jet literature provides insight into the characteristics of impinging diesel sprays.

Poreh *et al.* [15] studied an impinging air jet over a range of Reynolds numbers and found the velocity profiles within the spreading jet to be self-similar; that is, when the velocity profile at a radial location is normalized by the maximum velocity at that location and the distance from the wall is normalized by the height at which the velocity is half the maximum, the resulting dimensionless curve is independent of radial position. Moreover, the jet half-thickness was seen to increase nearly linearly with radial position, scaling with $h \sim r^{0.9}$. Self-similarity in impinging wall jets was also found by Knowles and Myszko [16], who report that self-similarity is achieved after a radial position $r \approx 3 \cdot d$, where d is the diameter of nozzle from which the free jet is injected. These results are for a distance from the injector to wall of $L = 10 \cdot d$. Relating the half-width of the wall jet $y_{1/2}$ (the distance from the wall to the point at which the radial velocity is half the maximum) to radial position, the authors report that the jet thickness grows linearly with radial position, and the rate of growth (captured by the wall jet spreading angle θ_r) tends to increase with increasing L.

Reduced-order spray models

Results from impinging diesel studies suggest that the mixing between fuel and air during impingement plays a large role in the combustion process. In this work, we describe the impingement process with a reduced-order model, which can be run more efficiently than time-intensive computational fluid dynamics (CFD) simulations.

Naber and Siebers's free spray model, developed for a steady gaseous jet, has been shown to accurately predict the penetration of non-vaporizing, and to a lesser extent vaporizing, diesel sprays [10]. Musculus and Kattke [17] extended the Naber and Siebers model to capture transient effects such as rate shaping and multiple injections by discretizing the spatial domain and solving the equations numerically. Pastor *et al.* [18] developed a 1-D model for an inert diesel spray, which was extended to capture reaction phenomena by Desantes *et al.* [19]. These models have been shown to predict the trends observed in diesel sprays.

Glauert [6] developed an analytical solution for a steady radially-spreading turbulent wall jet in 1956. Employing a matching procedure to couple solutions obtained with various turbulent viscosities for regions of the jet at various distances from the wall, the velocity distribution was found to not vary significantly throughout the jet. The jet thickness h was found to be proportional to $r^{1.015}$ and the velocity to decay with $r^{-1.14}$.

While useful for understanding the inner structure of the wall jet, such an analytical approach does not lend itself to the study of transient injection schedules or mixing after the end of injection. Thus, in this work, we take the control-volume approach of Musculus and Kattke [17], wherein the spray is discretized along the mean fluid path, and the internal structure of the spray is captured in constants which modify cross-sectionally averaged spray quantities. Simplifying slightly the wall jet geometry obtained with Glauert's solution, the spray thickness h is assumed to increase with radial position linearly, which is in rough agreement with data from Poreh *et al.* [15] and Knowles and Myszko [16].

The constants employed to capture the inner structure of the wall jet are obtained from an empirical correlation captured by Woods *et al.* [20]. This expression for the wall jet velocity profile was developed from wind tunnel measurements characterizing downdrafts in thunderstorms. As described, the 1-D approach taken in the current investigation does not require a high-fidelity representation of the inner structure of the wall jet, making empirically-determined correlations useful.

With this framework for a model, we simulate cases for which there is experimental data, showing the model captures observed trends yet over-predicts the wall spray's penetration. With this model, we then analyze the transient mixing characteristics of an impinging fuel spray, similar to the ways in which free sprays have been analyzed with reduced-order models. Finally, we present results from sweeps of injection parameters to identify mixing trend in diesel sprays.

Theoretical Development

The model of an impinging spray presented here consists of three separate segments: the free spray portion, in which the Musculus and Kattke control-volume model [17] is implemented; the turning region, in which the jet impinges on the wall and "turns" to begin spreading radially outward; and the radially-spreading wall jet portion, in which an approach similar to that utilized in the free spray portion is taken. Figure 1 shows a schematic of the model, including each of the three sections, lengths and angles, and axes names.

Free spray portion

Musculus and Kattke [17] developed a control volume-based model for a free diesel spray that conserves fuel mass and spray momentum throughout the spray. Discretized in space and solved stepping forward in time with timestep Δt, this approach captures transient effects such as injection rate shaping and end of injection (EOI) mixing phenomena.

Fuel mass is conserved along the free spray, leading to

$$m_{\text{f},i}^{t+1} = m_{\text{f},i}^t + \rho_{\text{f}} \left(\left(\beta \overline{\overline{X}}_{\text{f}} \overline{\overline{u}} A \right)_{i-1}^t - \left(\beta \overline{\overline{X}}_{\text{f}} \overline{\overline{u}} A \right)_i^t \right) \Delta t \tag{1}$$

for control volume i at timestep t. Spray momentum is conserved as well, with

$$M_{\text{f},i}^{t+1} = M_{\text{f},i}^t + \left(\left(\overline{\overline{\rho}} \beta \overline{\overline{u}}^2 A \right)_{i-1}^t - \left(\overline{\overline{\rho}} \beta \overline{\overline{u}}^2 A \right)_i^t \right) \Delta t. \tag{2}$$
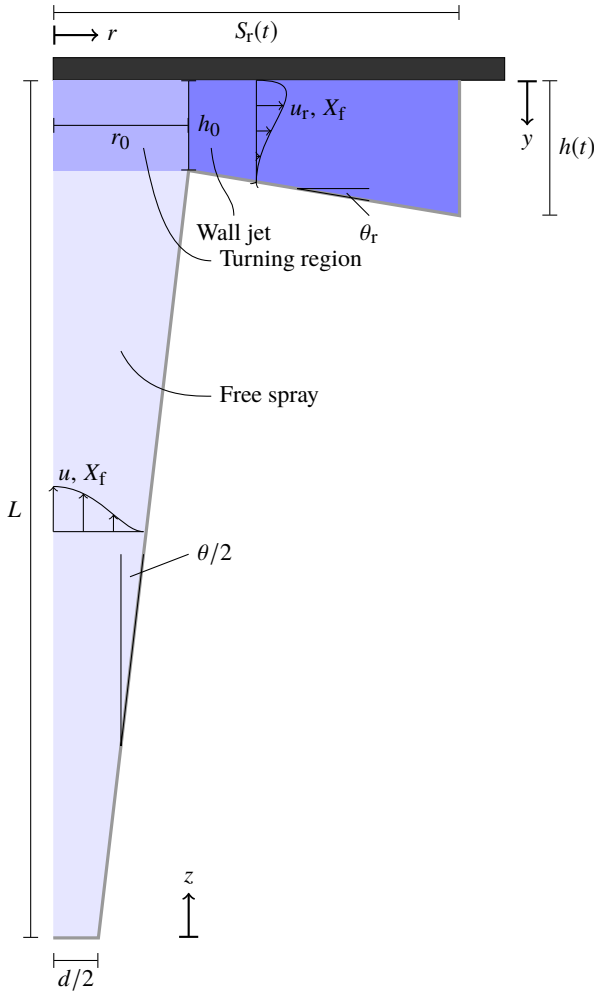
Figure 1: Schematic of the impingement model, including the free spray, turning, and wall jet regions. Important parameters and axes are marked.

The subscript "f" indicates a quantity for the fuel. β is a non-dimensional profile factor that in Equation (1) relates the product of the average velocity and fuel distribution profiles to the average of the product of the two profiles; in Equation (2), β serves as the momentum-flux correction factor and relates the square of the average velocity to the average of the squared velocity (as variations in spray density are neglected in the momentum calculation). The double-bars over fuel volume fraction X_f, spray velocity u, and spray density ρ signify the average of these values' time-averages over the spray cross-section. A is the area of the boundary between control volumes, which at a distance z from the injector is

$$A(x) = \pi \left(z \tan \theta/2\right)^2 \tag{3}$$

where θ is the spreading angle for the free spray. A jet's spreading angle is indicative of the rate at which it mixes with the ambient fluid; a larger θ indicates that the ambient and injected gases are mixed more readily.

Along the free spray axis, the velocity and concentration profiles follow the curve given by Abramovich,

$$\frac{\overline{X}_f}{\overline{X}_{f,c}} = \frac{\overline{u}}{\overline{u}_c} = \left(1 - \zeta^\omega\right)^2 \tag{4}$$

where the single bars designate time-averaged quantities, the subscript "c" designates the centerline quantity, ζ is the non-dimensional radial position $r/(z \tan \theta/2)$, and ω describes how far along the jet is in its transition from a top-hat shape, approaching $\omega = 1.5$ from ∞ as the jet develops.

The boundary condition for the model is the velocity of the jet at the nozzle, u_0.

Turning region

Once the free jet impinges on the wall, it is assumed that it immediately "turns" outward to begin spreading along the wall. The turning region, where this takes place, is modeled as a cylinder with radius r_0 and thickness h_0. The radius is determined from the spreading angle of the free jet θ and the length between the injector and the wall L (neglecting the thickness of the turning region), with

$$r_0 = L \cdot \tan \theta/2. \tag{5}$$

The turning region is shown in Figure 1. There are two unknowns that must be determined: the thickness h_0 and the average radial velocity of the fluid leaving the turning region, $\overline{\overline{u}}_{out}$. To solve for these variables, conservation of total mass, conservation of spray mass, and conservation of the fluid's kinetic energy are applied, which requires neglecting the frictional force exerted on the region by the wall. Conservation of mass implies that there is no entrainment of air into the turning region. Unlike the free spray, none of the surfaces surrounding the turning region interface with the ambient air, which indicates that no entrainment can take place. This also preserves the assumption that no diffusion or mixing takes place along the axis of the jet, which is an assumption that is used in both the Musculus and Kattke model as well as the wall model described here.

Neglecting pressure gradients within the turning region, as was done in the free spray by Musculus and Kattke [17], and the frictional force from the wall, the only force acting on the turning region is the normal force from the wall. Continuity requires the normal component of the fluid's velocity at the wall to be 0, so this normal force does not change the fluid's kinetic energy.

Mass is conserved in the turning region, which gives

$$\dot{m}_{in} = \dot{m}_{out}$$
$$\overline{\overline{\rho}} \cdot \overline{\overline{u}}_{in} \cdot A_{in} = \overline{\overline{\rho}} \cdot \overline{\overline{u}}_{out} \cdot A_{out}$$
$$\overline{\overline{u}}_{in} \cdot \left(\pi r_0^2\right) = \overline{\overline{u}}_{out} \cdot (2\pi r_0 h_0)$$
$$\overline{\overline{u}}_{in} \cdot r_0 = 2 \cdot \overline{\overline{u}}_{out} \cdot h_0 \tag{6}$$

when variations in the spray density across the cross-sections are neglected. Along with the total mass, fuel mass is conserved in the turning region, which gives

$$\dot{m}_{f\,in} = \dot{m}_{f\,out}$$
$$\overline{\overline{X}}_f \overline{\overline{\rho}} \cdot \beta_{in} \overline{\overline{u}}_{in} \cdot A_{in} = \overline{\overline{X}}_f \overline{\overline{\rho}} \cdot \beta_{out} \overline{\overline{u}}_{out} \cdot A_{out}$$
$$\beta_{in} \overline{\overline{u}}_{in} \cdot \left(\pi r_0^2\right) = \beta_{out} \overline{\overline{u}}_{out} \cdot (2\pi r_0 h_0)$$
$$\beta_{in} \overline{\overline{u}}_{in} \cdot r_0 = 2\beta_{out} \cdot \overline{\overline{u}}_{out} \cdot h_0. \tag{7}$$

Considered together, Equation (6) and Equation (7) require that $\beta_{out} = \beta_{in}$. Finally, we assume conservation of kinetic energy within the turning region, which gives

$$\overline{\overline{\rho}} \cdot \alpha_{in} \cdot \overline{\overline{u}}_{in}^2 \cdot A_{in} \overline{\overline{u}}_{in} = \overline{\overline{\rho}} \cdot \alpha_{out} \cdot \overline{\overline{u}}_{out}^2 \cdot A_{out} \overline{\overline{u}}_{out}$$
$$\alpha_{in} \overline{\overline{u}}_{in}^3 \left(\pi r_0^2\right) = \alpha_{out} \overline{\overline{u}}_{out}^3 (2\pi r_0 h_0)$$
$$\alpha_{in} \overline{\overline{u}}_{in}^3 r_0 = \alpha_{out} \overline{\overline{u}}_{out}^3 2h_0 \tag{8}$$

where α is the kinetic energy flux correction factor, which relates the cube of the average velocity to the average of the velocity cubed, and thus satisfies

$$\frac{\int_A \bar{u}^3 \, dA}{A} = \alpha \left(\frac{\int_A \bar{u} \, dA}{A} \right)^3 = \alpha \bar{\bar{u}}^3. \tag{9}$$

The correction factors for the free spray β_{in} and α_{in} can be calculated with the free-spray velocity profile, Equation (4). We have already determined that $\beta_{out} = \beta_{in}$, and α_{out} can be calculated with the method presented in the next section. Performing these calculations gives $\beta = \beta_{in} = 2.0195$, $\alpha = \alpha_{in} = 5.0736$, $\beta_r = \beta_{out} = 2.0195$, and $\alpha_r = \alpha_{out} = 4.7658$.

Then, with Equation (6) and Equation (8), we solve for the turning region parameters,

$$\bar{\bar{u}}_{out} = \bar{\bar{u}}_{in} \sqrt{\frac{\alpha_{in}\beta_{out}}{\alpha_{out}\beta_{in}}} \approx 1.03173 \cdot \bar{\bar{u}}_{in}, \tag{10}$$

$$h_0 = \frac{r_0}{2} \sqrt{\frac{\alpha_{out}\beta_{in}}{\alpha_{in}\beta_{out}}} \approx 0.48467 \cdot r_0. \tag{11}$$

The interaction between the coupled free spray and impingement models consists solely of the free spray model dictating the conditions at the inner-most region of the spreading wall jet, through the turning region relations described above. Thus, the model does not capture the effects the presence of the wall has on the free portion of the jet. However, Picket and Lopez [4] note that the combustion characteristics of a reacting spray is not affected by the presence of a downstream wall, and argue that this suggests the wall does not significantly impact ambient conditions in the free portion of the spray.

Wall-spreading portion

Whereas the free spray portion of the jet is modeled with cylindrical control volumes whose radii increase with axial position, the wall spray is modeled with ring-like control volumes whose radii and thickness increase with radial position. Figure 2 shows a schematic of the discretized spreading wall jet.
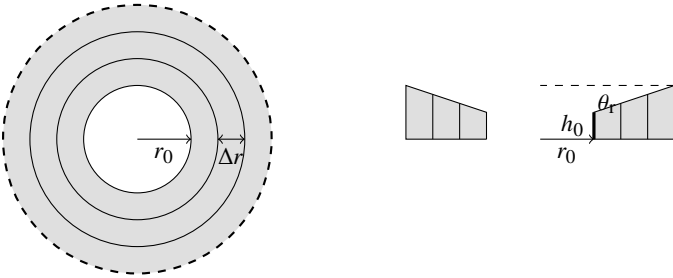

Figure 2: Schematics of the discretized impingement model: left, as viewed in the direction of the free spray; right, a cross-section as viewed in the radial direction.

Wood et al. [20] report that the velocity profile in a wall jet developed by an impinging jet fits the empirical correlation

$$\frac{u}{u_{max}} = 1.5 \cdot \left(\frac{y}{y_{1/2}} \right)^{1/6} \cdot \left(1 - \mathrm{erf} \left(0.70 \cdot \left(\frac{y}{y_{1/2}} \right) \right) \right) \tag{12}$$

where u_{max} is the maximum velocity at a given radial position and $y_{1/2}$ is the distance from the wall at which the velocity is half the maximum. In developing the free spray model, it was assumed that the normalized fuel volume fraction profile $\overline{X}_f/\overline{X}_{f,max}$ follows the same curve as the

normalized velocity profile (assuming the turbulent Schmidt number $Sc = 1$); that same assumption will be made again for the wall jet. This normalized profile is shown in Figure 3 along with the profile for the free spray from Equation (4).
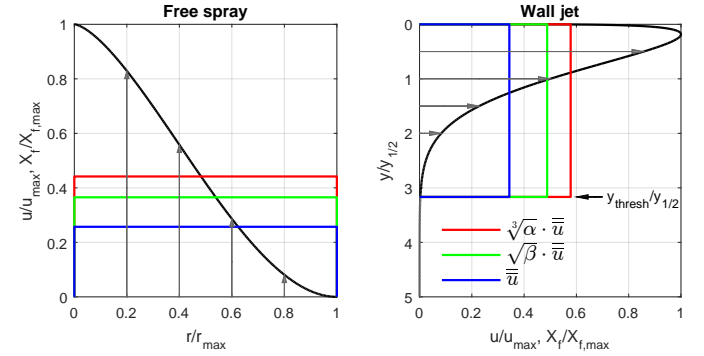

Figure 3: Velocity profiles for the free and wall jets (black). The mean velocity is shown in blue, while the corrected average velocity profiles for momentum and kinetic energy conservation are shown in green and red, respectively.

Additionally, experimental results from Poreh et al. [15] and Knowles and Myszko [16] suggest that the wall spray's growth follows $y_{1/2}/r \approx 0.10$. This relation allows us to calculate the radial spreading angle θ_r as a function of some threshold velocity which defines the thickness of the spray: for a given threshold velocity $\bar{u}_{thresh}/\bar{u}_{max}$, we can calculate the corresponding distance from the wall $y_{thresh}/y_{1/2}$ with Equation (12). Since we know from experiments that $y_{1/2}/r \approx 0.10$, we can calculate the growth rate of our "threshold" thickness with

$$\frac{y_{thresh}}{r} = \frac{y_{1/2}}{r} \cdot \frac{y_{thresh}}{y_{1/2}} = 0.10 \cdot \frac{y_{thresh}}{y_{1/2}}. \tag{13}$$

The radial spreading angle with this threshold velocity is then

$$\theta_r = \arctan \left(0.10 \cdot \frac{y_{thresh}}{y_{1/2}} \right) \tag{14}$$

The next matter is to determine a suitable threshold velocity $\bar{u}_{thresh}/\bar{u}_{max}$ with which to define the outer boundary of the wall jet. From conservation of total mass and fuel mass within the turning region, we have determined that the profile factor for the wall jet, β_r, must equal that for the free spray, β. β_r is calculated with

$$\beta_r = \frac{\int_A \bar{u}^2 \, dA/A}{\left(\int_A \bar{u} \, dA/A \right)^2} = \frac{\int_A \bar{u}^2 \, dA/A}{\bar{\bar{u}}^2}. \tag{15}$$

The numerator of Equation (15) will depend on our choice of $\bar{u}_{thresh}/\bar{u}_{max}$, which determines $y_{thresh}/y_{1/2}$. With iteration, we find that using a threshold value $\bar{u}_{thresh}/\bar{u}_{max} = 0.00323$ to define the edge of the wall jet gives $\beta_r = \beta = 2.0195$. With Equation (14), we find the corresponding spreading angle is $\theta_r = 17.572°$.

The portion of Wood's velocity profile included in this definition of the spray, between $y = 0$ and $y = y_{thresh}$, is shown in Figure 3. Also shown is the average velocity over the y range considered as the spray (in blue), as well as the corrected average velocity profiles for momentum flux (green) and kinetic energy flux (red).

With the wall jet geometry and correction factors defined, we can apply the fuel mass and spray momentum conservation equations. Fuel mass conservation gives

$$m_{f,i}^{t+1} = m_{f,i}^t + \rho_f \left(\left(\beta_r \overline{\overline{X}}_f \bar{\bar{u}}_r A \right)_{i-1}^t - \left(\beta_r \overline{\overline{X}}_f \bar{\bar{u}}_r A \right)_i^t \right) \Delta t. \tag{16}$$

where A is the cross-sectional area of the spray and is given by

$$A = 2\pi r \cdot (h_0 + (r - r_0) \cdot \tan \theta_r). \qquad (17)$$

Again neglecting variations in spray density across the spray cross-sections in the momentum calculation, β_r now serves as a momentum-flux correction parameter, and the momentum conservation expression is

$$M_{f,i}^{t+1} = M_{f,i}^t + \left(\left(\overline{\overline{\rho}} \beta_r \overline{\overline{u}}_r^2 A \right)_{i-1}^t - \left(\overline{\overline{\rho}} \beta_r \overline{\overline{u}}_r^2 A \right)_i^t \right) \Delta t. \qquad (18)$$

Experimental Results and Model Verification

The proposed model is compared to two sets of experimental data: gas jet experiments and diesel spray experiments. Results from gas jet impingement tests are presented in this section. The experimental data is then used to compare to the impingement model, which is finally applied to diesel conditions to characterize entrainment phenomena in impinging diesel sprays.

Experimental setup

The experiment system employed is that which is described in greater detail in [21].

Injection system

The gas injection system follows that of Abani and Ghandhi [12] and is shown in the Figure 4. A valve, connected to a regulator on a pressurized tank of helium, controls the flow of the helium into the injector, which consists of a small mixing volume on top of which an orifice plate is affixed.
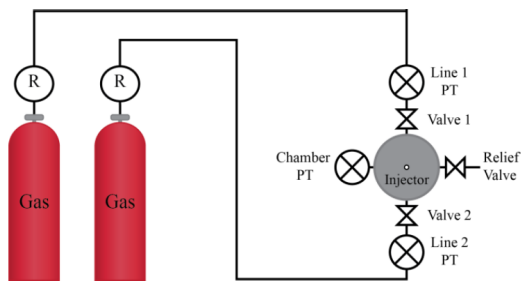
Figure 4: Schematic of the injection system [13], shown with a second valve and relief valve which were not employed in this investigation. The gas injector and flat plate suspended above it (not shown) are situated in the open in a laboratory.

Gas flow is controlled by ASCO Red Hat solenoid valves, which are actuated by a program developed in LabVIEW and executed on a National Instruments NI-RIO 9024 data acquisition system. Normally closed, the valves are opened by passing current through the solenoids, producing a magnetic field which lifts the rod which had restricted flow. The valves are observed to have "opening times" of approximately 10 ms.

The nozzle is drilled into an orifice plate which rests on top of the injector. The nozzle is a 1 mm hole with $L/D = 3$. The velocity coefficient was determined to be $C_v \approx 0.8$ [21].

The plate onto which the gas jet impinges is suspended vertically above the injector with a tripod whose central rod is inverted in comparison to its typical configuration for photography. The plate is large enough that the spreading jet does not approach the edges during the recorded videos.

Schlieren imaging system

A z-type schlieren imaging system is used to visualize gaseous jets. As collimated light passes through a region of varying density such as a gaseous jet, rays are deflected due to the dependence of a gas's refractive index on its density. When the light is then focused onto a knife edge, such that a portion of the light is blocked, certain rays that would have missed the knife edge now hit it, and others that would have hit it now miss it, due to the rays' deflections. The result is an image which visualizes the density gradients in the region through which the light has passed. The use of a vertical knife-edge cutoff results in the image intensity corresponding to density gradients in the horizontal direction. This is desirable in studying gas jets as the jets are injected vertically. Light is collimated from a point source and re-focused onto the knife edge with two 6 in-diameter mirrors. The "viewing window" in which the jets are visualized is then a 6 in-diameter circle parallel with the plane in which the gas is injected.

Injection sequences are recorded at 15 000 fps with a high-speed Photron SA1.1 camera. The frame resolution is 504 by 704 pixels. The spatial calibration is determined by measuring the number of pixels corresponding to the width of the injector block, which is visible in the recorded frames. Statistical analysis showed that averaging an ensemble of 20 tests for each case considered results in sufficiently accurate data [21], so unless otherwise noted, 20 runs are recorded and averaged for each case.

Data analysis

The first step in image processing is background subtraction, which serves to remove noise and experiment hardware from the images and have an intensity of 0 correspond to 0 density gradient. To obtain a background image, 30 blank frames are recorded before the start of the first injection for each run. These 30 frames are averaged and subtracted from each frame in the movie. After background subtraction, positive and negative values of pixel intensity correspond to opposite directions of density gradient normal to the injection axis. In order to determine the region of the image occupied by the jet, the absolute value of each image is then taken, such that the pixel intensities correspond to the magnitude of the horizontal density gradients.

After this process has been done to each of the 20 test runs obtained, the movies are "shifted" such that the SOI is aligned based upon the the pressure curves. The corresponding frames from each movie are then averaged, as are the shifted pressure traces.

The tips of the free jet and left and right sides of the wall jet are tracked in each of the original 20 tests, defining the tip location as the farthest downstream location containing a pixel intensity over some threshold, shown in Figure 5. Results from the individual tests are averaged to produce the ensemble-averaged result given for the case. A similar process is applied to track the thickening of the jet away from the wall, but due to the weaker signal in this region, this is only done once, with the ensemble-averaged frames.
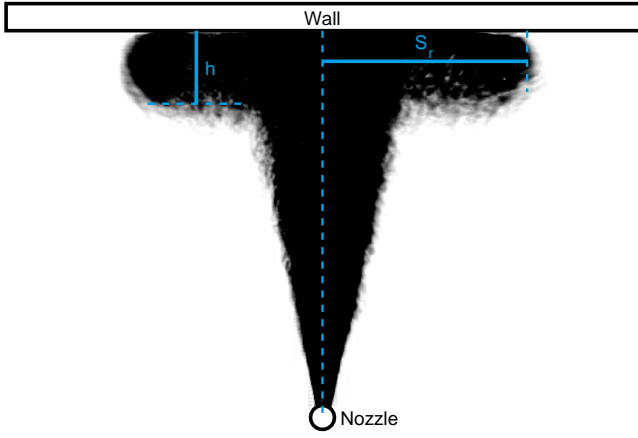
Figure 5: Schematic of the wall spreading determination, overlaid on a frame after impingement. The reported values for h and S_r are the averages of those determined in the left and right sides of the jet (only the left-side calculation of h and the right-side calculation of S_r are shown).

Injection profiles

Figure 7 shows the recorded pressure traces for each case. The steady-state injection pressure is reached at about 5 ms after the start of injection. Slight variations in the maximum pressure attained for the nominally $40\,\mathrm{kPa_g}$ cases are due to the two sets of $40\,\mathrm{kPa_g}$ not being run back-to-back.
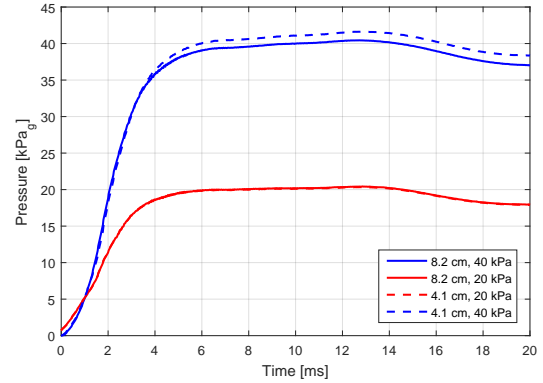
Figure 7: Chamber pressure traces for the four impingement conditions.

Gas jet wall impingement results

To study the development of impinging jets, helium is injected at two pressures towards a flat plate perpendicular to the injection axis at two distances from the injector. Thus, four conditions are run, with $L = 8.2$ and 4.1 cm and $P_{inj} = 40$ and $20\,\mathrm{kPa_g}$. The nozzle diameter is $d = 1$ mm. Each curve plotted is the average of the data obtained in 20 runs, except for the $L = 4.1$ cm and $P_{inj} = 40$ kPa case, from which the schlieren timing for one run was determined to be erroneous. Ensemble-averaged schlieren images of the impinging sprays are shown in Figure 6, with frames overlaid in 1 ms intervals after the start of injection.

To compensate for the higher density of the air initially in the chamber, which causes the jet to have greater initial momentum, an effective velocity is calculated as described in the Appendix, and this effective velocity is used as the boundary condition to the spray model.

Free penetration and spreading profiles

Figure 6 shows the ensemble-averaged wall impingement results, with color-coded frames shown in 1 ms increments. The color-coding is constant between cases. Frames were combined by overlaying the frames in opposite order and specifying their local transparency as a function of the image intensity.

Figure 6: Impinging jet development at various injection pressures and wall distances. Frames are overlaid in 1 ms intervals.

The dark-red frame shows the jet as it first emerges from the nozzle. Comparing the higher-pressure jets to the lower-pressure ones, at a given time after the start of injection, the higher-pressure jets have penetrated farther than the lower-pressure ones. Once impingement occurs, the head of the jet begins to fill out the volume around the impingement point. As the jet spreads further, it increases in both radial distance from the impingement point (S_r) and thickness away from the plate (h). Note that as the jet spreads, it is assumed that the cross-sections retain the shape shown in Figure 1; this is not apparent in the frames shown, since the schlieren technique provides a line-of-sight view of the jet.

The penetration rates of the free and wall jets and the thickening rate of the wall jet were tracked and are plotted together in Figure 8 against time. The inflection point in the free-jet penetration curves is possibly caused by the transient composition of the injected gas. The jets spread much more slowly along the wall than they do in the free jet portion, and the wall jet thickening is even slower.
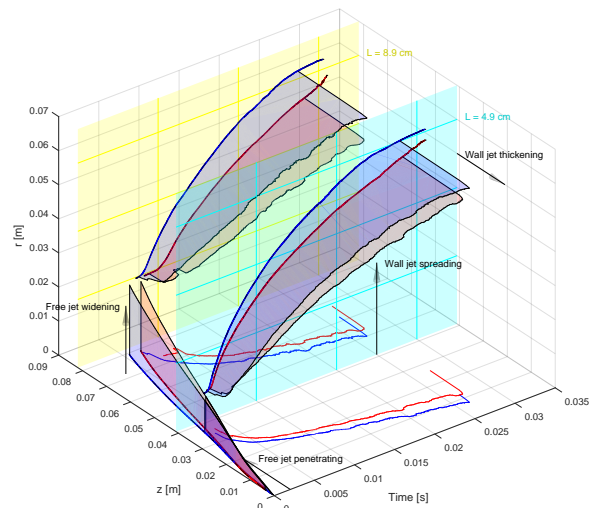

Figure 9: Experimental data with the distances plotted on planes corresponding to those in which they were measured. Red cases correspond to $P_{inj} = 20\,\text{kPa}_g$ and blue cases correspond to $P_{inj} = 40\,\text{kPa}_g$.

from each curve represent the widening or thickening of the jet in the direction orthogonal to the plotted penetration direction. For the free spray, then, the surface height represents the jet's widening in the r direction (given its conical structure). For the wall jet, the surface distance represents the thickening of the jet back towards the injector in the $-z$ direction.

Viewing any set of free and wall jet surfaces in the r–z plane gives half the cross-section of the spray, provided that the images captured during the jet penetration are indicative of the steady-state structure of the jet. This visualization provides insight into the structure of the spray that is not apparent in the schlieren images, which visualize the projection of the entire spray (not just a cross-section). Imagining this projection in the r–z plane revolved around the z axis, it is apparent that the wall jet occupies a much greater volume than the free jet.

Initial thickness and wall spreading angle calculations

The thickness of the spreading jet is plotted against the wall jet's radial penetration in Figure 10. As expected, once the spreading jet reaches a steady state, thickness increases nearly linearly with wall penetration. Also shown in Figure 10 are the linear fits applied to this steady region, which is defined as starting once the jet spreads 1.5 cm beyond r_0 end ending at $r = 5.5$ cm. The projected initial thickness h_0, defined as the value of the fit at r_0, and spreading angle θ_r, defined as the arctangent of the slope of the linear fit, are given in Table 1.

Figure 8: Recorded free penetration, wall penetration, and thickness profiles for each gas jet impingement case.

A "dwell time" between impingement and the start of radial spreading is observed. This is likely caused by the head of the jet first expanding to fill the turning region before beginning to spread radially, which is seen in the visual results in the snapshots just after the jet first impinges along the wall. The corresponding initial abrupt increase in h results from the head of the jet "filling out" in the turning region just after impingement.

Figure 9 shows the free jet penetration, free jet widening (calculated by $S \cdot \tan \theta/2$), wall jet spreading, and wall jet thickening, with the z and r directions oriented perpendicular to each other as the corresponding directions are in the experiment. This visualization is useful in relating the rates of free jet penetrating, free jet widening, wall jet spreading, and wall jet thickening.

The wall spreading is plotted on a plane orthogonal to the one on which the free jet penetration is plotted, since along the wall the jet spreads perpendicular to its original injection direction. The surfaces extending

Table 1: Experimentally-determined wall jet properties

P_{inj} [kPa$_g$]	L [cm]	h_0 [cm]	θ_r
40	8.2	1.13	21.1°
20	8.2	1.04	23.4°
20	4.1	0.83	19.8°
40	4.1	0.74	20.0°

In the region just after impingement, the wall jet is not as thick as is predicted by the linearly-increasing assumption. This is likely a transient effect due to the jet not being fully developed when it is measured in this region. An analogous phenomena in free sprays is the initial transient variation seen in the free jet spreading angle θ just after start of injection shown by Borz *et al.* [13].
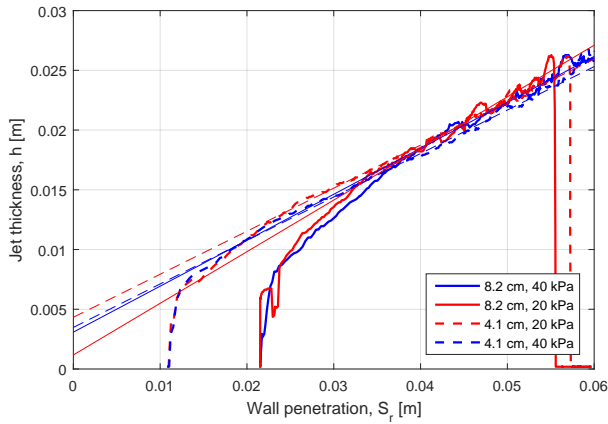
Figure 10: Jet thickness plotted against wall penetration for each case. Also shown as the thin lines are the linear fit applied between $r_0 + 1.5$ cm and 5.5 cm along the wall.

Both θ_r and h_0 are seen to correlate more with L than P_{inj}. As is suggested by Equation (11), the initial thickness h_0 is dependent primarily on r_0, which with a constant free jet spreading angle is solely dependent on L. The agreement between values calculated for h_0 for different pressures with the same L supports the kinetic energy conservation assumption applied to the turning region. Additionally, the positive correlation between θ_r and L agrees with gas jet results from Knowles and Myszko [16].

Entrainment characteristics of the spreading wall jet

Figure 11 shows the penetration rates of the radially-spreading wall jets. The rates were constructed by smoothing the wall penetration curve S_r with a five-point moving average scheme and differentiating with respect to time.
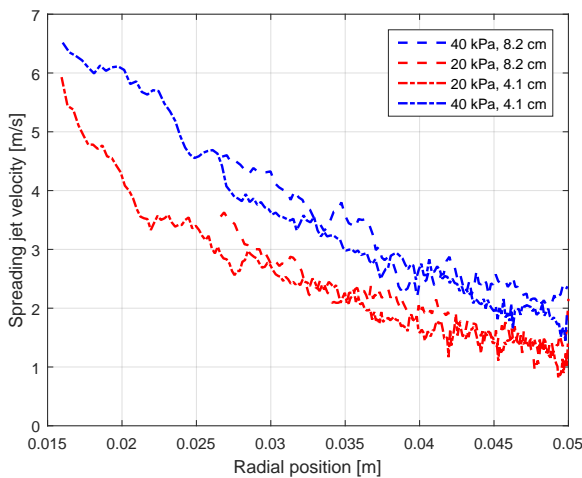
Figure 11: Radial penetration rates for the spreading wall jets.

From the radial penetration rate profiles, we see that for a given wall distance L, the penetration rate at a given position along the wall increases with increasing injection pressure. The radial velocity does not, however, show a strong dependence on L.

Simulation of impinging gas jets

Experimental results are here compared with the simulation results of the model presented earlier in this paper. Simulation results are obtained numerically with Matlab. Spray penetration from simulation results is calculated at each timestep by identifying the farthest-downstream control volume in which the fuel volume fraction is above some threshold. Figures 12 and 13 show the measured and predicted free and wall penetration curves for the jets at the four conditions investigated.

Table 2 compares the measured values of h_0 to those calculated with Equation (11). A comparison between predicted and measured $\bar{\bar{u}}_{out}$ is not made here, as the steady-state velocity in the jet cannot be accurately determined from schlieren measurements.

Table 2: Comparison of measured and predicted h_0

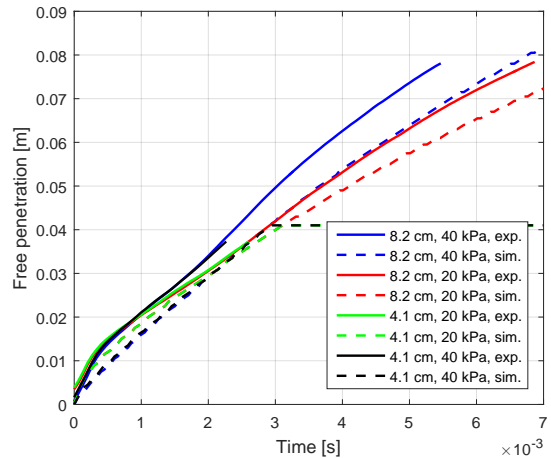| P_{inj} [kPa$_g$]	L [cm]	measured h_0 [cm]	predicted h_0 [cm]
40	8.2	1.13	0.80
20	8.2	1.04	0.80
20	4.1	0.83	0.40
40	4.1	0.74	0.40

Figure 12: Model and experimental free penetration results for gas jets.
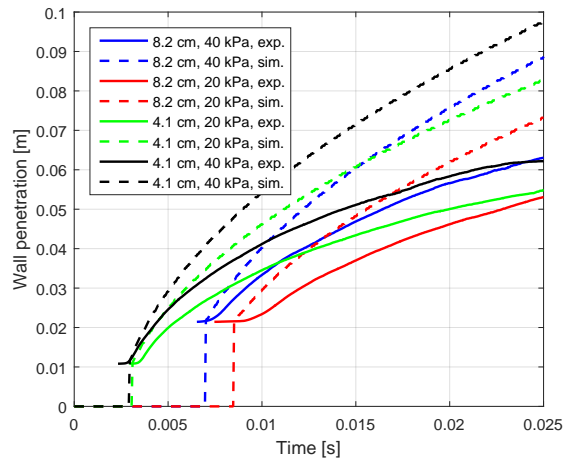

Figure 13: Model and experimental wall penetration results for gas jets.

The kinetic energy flux conservation employed in calculating h_0 underpredicts the initial wall jet thickness. This may be because the assumed velocity profile used in calculating α_{out} is not representative of the initial portion of the wall jet; indeed, Wood *et al.* [20] report that the self-similar profile is reached some distance downstream of the

impingement point. Another explanation for the discrepancy is that the thickness profile shown in Figure 10 (with which h_0 is determined) is not representative of the steady-state thickness profile in the wall jet.

Additionally, we see that the model over-predicts the penetration of the wall jet by nearly a factor of 2. This is likely because friction between the spray and wall was neglected in the theoretical development of the model; in reality, the velocity gradient near the wall imposed by the no-slip condition will result in frictional losses that slow the wall jet.

Analysis of diesel conditions

Comparison to impinging diesel data

Model results are here compared to experimental data from Zhang *et al.* [5], who studied the impingement of non-reacting diesel sprays onto a flat plate over a range of injection pressures (P_f = 100 MPa, 240 MPa and 300 MPa), nozzle hole diameters (d_{noz} = 0.08 mm, 0.1 mm and 0.16 mm), and ambient densities (ρ_a = 11 kg/m^3 and 15 kg/m^3). The injection duration was varied with injection pressure, with durations of t_{inj} = 2.2 ms, 1.4 ms and 1.3 ms corresponding to the pressures P_f = 100 MPa, 240 MPa and 300 MPa, respectively. Zhang's data was obtained graphically from Figure 5 in [5].

The value used for the free spray spreading angle is θ = 22°. Spray penetration is reported as the sum of the axial and radial spray penetrations; i.e., $S_{combined} = L + S_r$ after impingement. The "jump" seen in the plots of simulated combined penetration correspond to the head of the jet moving from the impingement point to a position of r_0 along the wall (from a combined penetration of L to $L + r_0$). A comparison between experimental data and simulation results is given in Figure 14.

The model is seen to over-predict the penetration of the wall spray. In comparison with Figure 11 in [5], we see that the Glauert correlation under-predicts the penetration. Zhang *et al.* note that sprays from micro-hole nozzles (the smaller two of the three investigated) behave more closely to the gas jets modeled by the Glauert correlation. This trend is not seen with comparison to our control-volume based model: with the larger nozzle, the slopes of the predicted penetration curves appear to better match those of the experimental data.

The over-prediction of the diesel spray wall jet penetration is less severe than was seen for the gaseous jets, shown in Figure 13. Attributing discrepancies between the model and experimental data to the model's omission of wall friction, this suggests that ignoring wall friction may be a more acceptable assumption to make in modeling diesel sprays than the low-pressure gas jets studied in this investigation.

Characterization of impingement phenomena

In this section, results from a single simulation (Spray A conditions, with a wall located at L = 4 cm from the nozzle) are analyzed to identify important impingement and mixing phenomena. Plots of several quantities are shown, and important events in each are labeled and discussed.

At each time t, the local entrainment rate in the sprays is computed with

$$\frac{\partial \dot{m}_e(x,t)}{\partial x} = \rho_a \frac{\partial}{\partial x}\left(\bar{\bar{u}}(x,t)A(x)\right) \quad (19)$$

where x is the direction in which the spray is propagating (z for the free spray and r for the wall spray) and $A(x)$ is the cross-sectional area of the control volumes. This local entrainment rate has dimensions of kg$_a$/s/m, where the "a" subscript indicates the ambient gas. A more
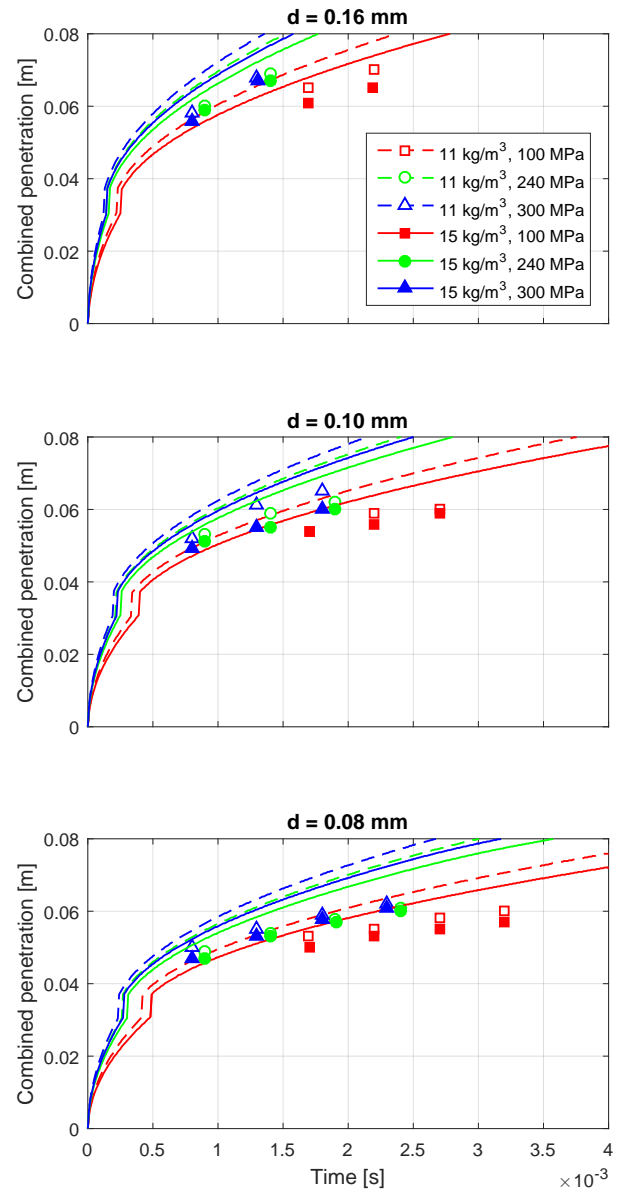

Figure 14: Experimental diesel wall impingement data (from [5], shown with markers) and simulation results with the model presented in this paper (shown with lines).

relevant quantity to combustion analysis may be the entrainment rate at a point, normalized by the quantity of fuel at that point [17]. This fuel-specific entrainment rate has units of s^{-1} and is calculated with

$$\frac{\partial \dot{m}_e}{\partial m_f}(x,t) = \frac{\frac{\partial \dot{m}_e}{\partial x}(x,t)}{\frac{\partial m_f}{\partial x}(x,t)}. \quad (20)$$

The instantaneous entrainment rate profiles $\frac{\partial \dot{m}_e}{\partial x}(x,t)$ are shown in the top of Figure 15. The bottom of Figure 15 shows the fuel-specific entrainment rate profiles, $\partial \dot{m}_e/\partial m_f(x,t)$, which may be more relevant to combustion analysis as the desired entrainment rate at a point is likely a function of the local quantity of fuel.
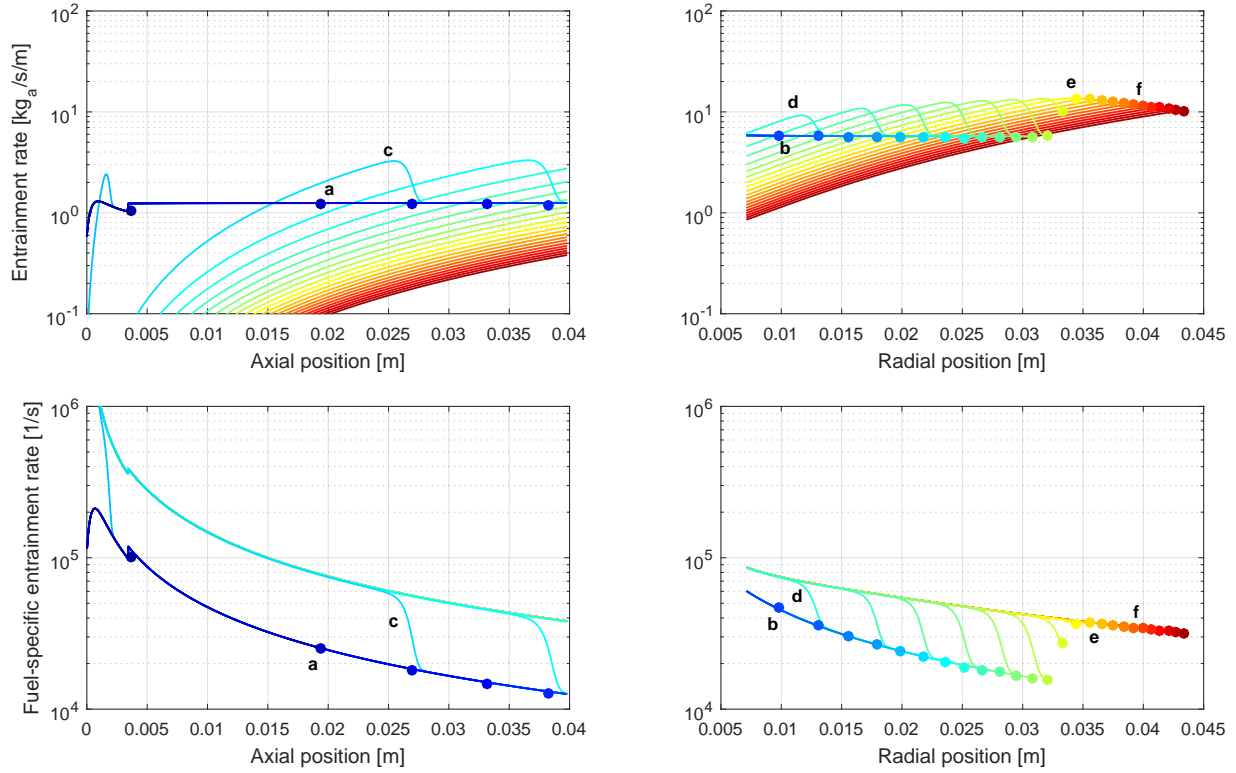
Figure 15: Evolution of entrainment (top) and fuel-specific entrainment (bottom) rates for the free (left) and wall (right) sprays. Each colored curve corresponds to the entrainment profile at a point in time; the color-time mapping is shown in the bottom of Figure 16. Letters correspond to specific times that are discussed below.

To compute the total spray entrainment rate as a function of time, the local entrainment rate is integrated over the spray at each point in time (from the nozzle to the spray tip), yielding the total spray entrainment rate as a function of time, with

$$\dot{m}_e(t) = \int_0^{S_x(t)} \frac{\partial \dot{m}_e(x,t)}{\partial x} dx. \tag{21}$$

These rates for the free spray, wall spray, and the combination of the two are shown in Figure 16. Also shown here are the times corresponding to the colors used in Figures 15 and 17. Finally, Figure 17 shows the fuel volume fraction profiles in the free and wall sprays $\overline{\overline{X}}_f(x,t)$ at different times.
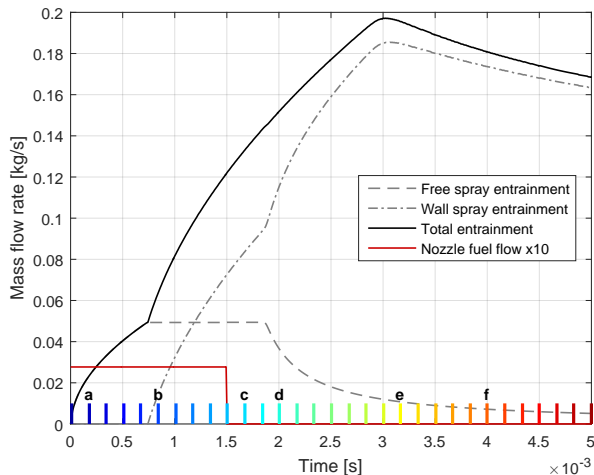
Figure 16: Entrainment rates and fuel flow rate as functions of time. The colored bars specify the times corresponding to curves shown in Figures 15 and 17.

Significant points in time, corresponding to the times labeled **a** - **f** in Figures 15 - 17, are described below.

a) The spray has not yet reached the wall, such that the fuel volume fraction abruptly drops off at the head of the spray but follows the steady-jet profile upstream of the head.

b) Prior to the end of injection, the spray has impinged upon the wall and begun to spread radially outwards.

c) Shortly after EOI, the entrainment wave [17] has propagated through a portion of the free spray, increasing entrainment and decreasing fuel concentration. At this point, the wave is not yet "felt" in the spreading jet, as points in the spray downstream of the head of the entrainment wave remain at their steady-jet fuel concentrations.

d) The entrainment wave has passed through the entire free spray and reached the spreading jet. An increase in entrainment in the spreading jet is accompanied by a decrease in entrainment in the free spray.

e) The entrainment wave reaches the tip of the spreading jet, and the fuel volume fraction is below its steady-jet value at every point in the free and radial sprays. The fuel-specific entrainment rate profiles at all following times are that of the post-entrainment wave jet.

f) The radial spray continues to penetrate outwards (at a slower rate) as the fuel concentration continues to drop throughout.

In both the free and wall sprays, there are two distinct fuel-specific entrainment curves seen in the bottom of Figure 15, corresponding to before and after the arrival of the entrainment wave. Thus, the only time dependence of this normalized entrainment rate at a given point in the spray is the matter of whether or not the entrainment wave has passed
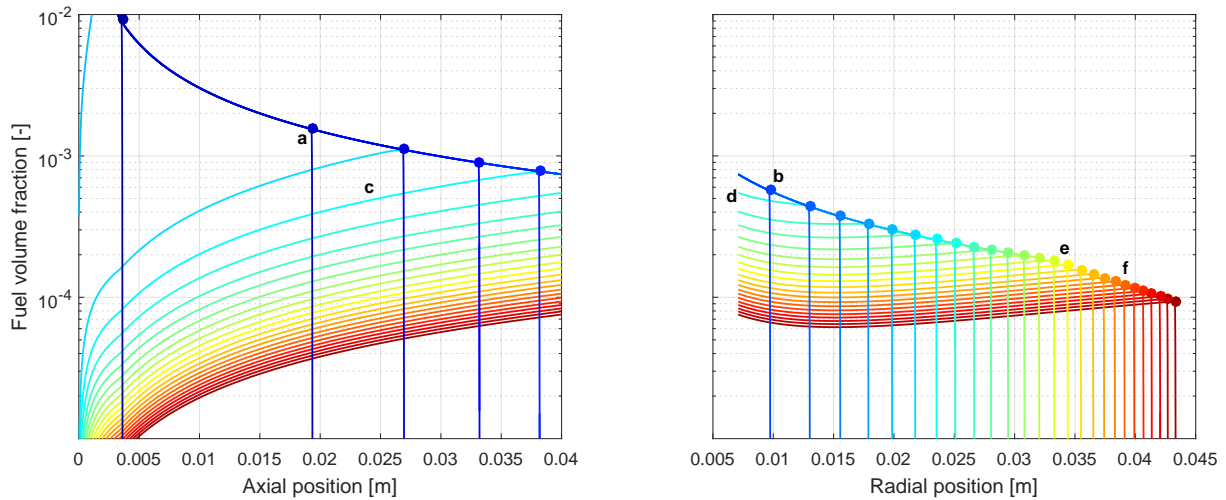
Figure 17: Evolution of fuel volume fraction distribution in the free (left) and wall (right) sprays. Each colored curve corresponds to the fuel distribution at a point in time; the color-time mapping is shown in the bottom of Figure 16.

yet. As the entrainment wave passes a point, the normalized entrainment rate merely "jumps" up from the pre-wave curve to a greater value on the post-wave curve.

After the entrainment wave has reached the spreading jet, a local minimum in fuel concentration is found at some intermediate position in the spray, and there is not a strong spatial dependence on fuel concentration within the wall jet as there is in the free spray. The presence of the wall clearly results in an increase in total spray entrainment: the spreading jet more readily entrains ambient air than the free spray does. Unlike in the free spray, the fuel concentration in the wall jet remains relatively uniform spatially after the arrival of the entrainment wave. Musculus and Kattke reported that the entrainment wave propagates through a free spray at approximately twice the rate of the initial spray penetration; this result is seen again in this wall spray simulation, as the entrainment wave reaches the tip of the spreading jet in half the time (1.5 ms) than it took the tip to reach that position from the nozzle (3 ms).

Evidenced by the continuation of the constant free spray entrainment rate after EOI in Figure 16 (just after time **c**), as the entrainment wave passes through the free spray, total entrainment is not affected, since the local increase in entrainment in an entrainment wave is accompanied by an upstream decrease in local entrainment. However, in comparing the curves corresponding to time **c** in Figures 15 and 17, the upstream region of the spray, in which the entrainment rate is lower than the steady-jet value, is the same region in which the fuel concentration is significantly lower than the steady-jet value (and therefore where entrainment is less likely to be desired, to prevent over-leaning, which can result in high emissions [22]). Thus, while the total entrainment rate in the free spray is not affected by the entrainment wave, the entrainment wave *distributes* the entrainment more effectively throughout the spray.

Global entrainment characteristics over a range of combustion parameters

In this section, the coupled free spray/wall spreading model is run over a range of diesel-like conditions and geometries, and the global entrainment impacts are compared between configurations. A sweep of operating conditions is made around the Engine Combustion Network Spray A condition, with wall distances of $L = 3$ cm, 5 cm and 7 cm. The range of parameters swept is given in Table 3.

Table 3: Engine conditions swept.

Parameter	Value
P_f	1500 bar to 3000 bar
EOI	1.5 ms
d_{noz}	0.090 mm
ρ_f	850 kg/m^3
θ	20°
ρ_a	22.8 kg/m^3
L	3 cm to 7 cm

Effect of wall distance

The first set of simulations analyzed is that in which the fuel injection pressure is held at $P_f = 2250$ bar as L is varied. Figure 18 shows the wall penetration curves for these cases, and Figure 19 shows the instantaneous entrainment rate. The wall jet spreads the fastest when the wall is closest to the injector, but the highest entrainment rates are achieved when L is the greatest.
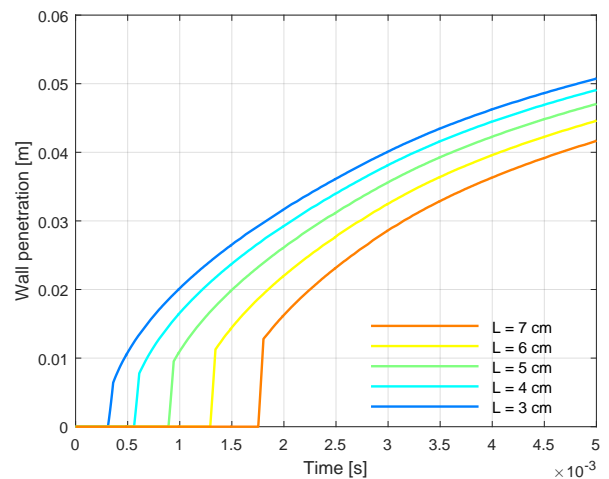

Figure 18: Wall penetration profiles as a function of time with $P_f = 2250$ bar and various L and θ_r.
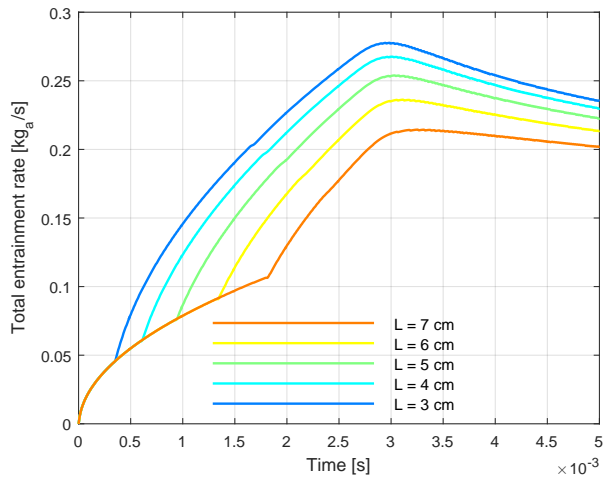
Figure 19: Total entrainment rate as a function of time with $P_f = 2250$ bar and various L.
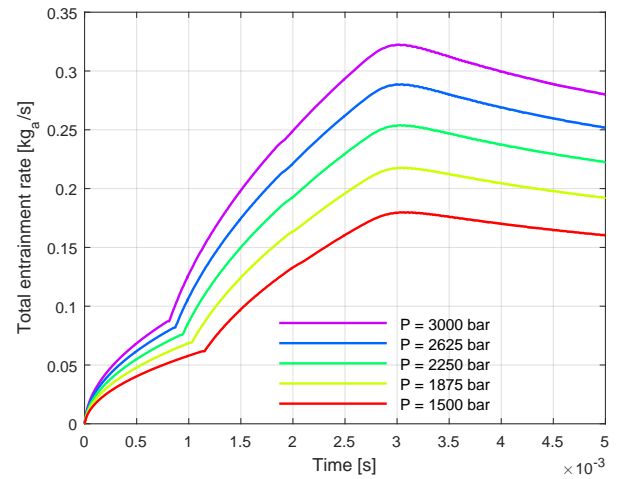

Figure 21: Total entrainment rate as a function of time with $L = 5$ cm and various P_f.

Effect of injection pressure

Here, the wall distance is held constant at $L = 5$ cm while P_f is varied. Figure 20 shows the wall penetration curves for these cases, and Figure 21 shows the instantaneous entrainment rate.
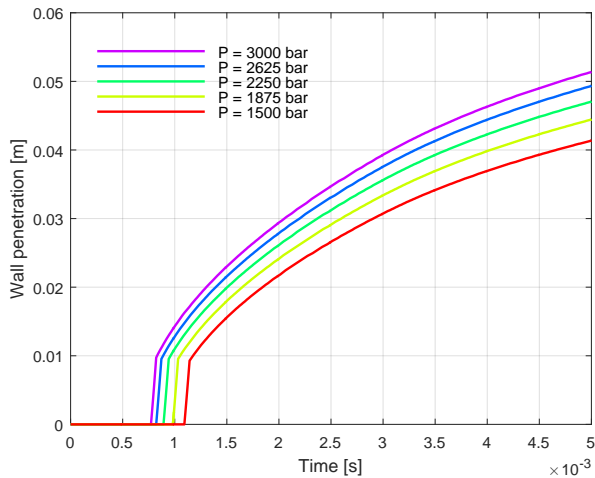

Figure 20: Wall penetration profiles as a function of time with $L = 5$ cm and various P_f.

The wall jet spreads the fastest when the injection pressure is the greatest. When P_f is decreased, the wall jet penetrates more slowly. The highest entrainment rates are achieved when P_f is the greatest.

Conclusions and Future Work

This paper has outlined a new formulation for capturing the penetration and mixing of diesel sprays after wall impingement by modeling the spray as a gaseous jet. The model breaks the spray into three regions: a free-jet region, a turning region, and a wall-jet region. The free-jet region follows the formulation of Musculus and Kattke [17], which includes the ability to capture changes in entrainment as a result of starting and stopping profiles of the spray. The turning region uses conservation of energy to calculate the conditions of the spray as it impacts the wall and begins to spread along the wall surface. The wall-jet region uses the profile from Wood *et al.* [20] to model the behavior of the wall jet, calculating both penetration rate and entrainment during this portion of the spray. The model captures trends from both gas jet and diesel spray experiments as a function of injection pressure and distance from the injector to the wall. Results suggest that entrainment rates are greater along the wall than in the free spray, and that the entrainment wave [17] propagates through the wall jet more quickly than the head of the jet initially penetrates, as is the case in the free spray.

There are three key outcomes of this work. First, a tractable model for diesel sprays has been extended from the free-spray regime to the wall-jet regime. In both small-bore and large-bore diesel engines, spray-wall interaction occurs during a significant portion of the duration of the injection, and so having a reduced-order model to capture this phenomenon is useful. Second, this formulation allows for the estimation of entrainment along the wall jet, which could be useful in understanding the progression of the fuel-air mixture in this region. A model like the one proposed here can help to better understand the air entrainment into this region and the impact of injection profiles and duration on mixing at the wall. Third, the model can be used for initial parameter studies of injection profiles, injection duration, and bowl diameter (distance between the injector and the wall), to understand the impact that these parameters have on the penetration and mixing characteristics of the jet along the wall.

Further development of the model is required in order to improve its predictive accuracy. First, friction along the wall should be taken into account in the wall-jet model in order to better predict the spreading rate and entrainment in that region. While the assumed velocity profile along the wall accounts for friction in one way, it is not taken into account in the momentum conservation equation in the current formulation. Future iterations will include this term. Additionally, we have made the assumption of unity Schmidt number in all portions of the jet (free spray,

turning region, and wall jet). This follows the formulation by Musculus and Kattke for the free-jet, but it is unclear if this assumption is valid, particularly along the wall. Unfortunately, the wall-jet literature does not provide significant insight into the scalar turbulence in a wall jet, and so further investigation into this phenomenon is required.

References

[1] United States Environmental Protection Agency, "Regulations for Smog, Soot, and Other Air Pollution from Commercial Trucks & Buses," https://www.epa.gov/regulations-emissions-vehicles-and-engines/regulations-smog-soot-and-other-air-pollution-commercial.

[2] United States Environmental Protection Agency, "Regulations for Greenhouse Gas Emissions from Commercial Trucks & Buses," https://www.epa.gov/regulations-emissions-vehicles-and-engines/regulations-smog-soot-and-other-air-pollution-commercial.

[3] Li, K., Nishida, K., Ogata, Y., and Shi, B., "Effect of flat-wall impingement on diesel spray combustion," Proceedings of the Institution of Mechanical Engineers, Part D: Journal of Automobile Engineering 229(5):535–549, 2015, doi: 10.1177/0954407014547242.

[4] Pickett, L. M. and López, J. J., "Jet-Wall Interaction Effects on Diesel Combustion and Soot Formation," SAE 2005 World Congress & Exhibition 2005(724):1–17, 2005, doi: 10.4271/2005-01-0921.

[5] Zhang, W., Nishida, K., Gao, J., and Miura, D., "An experimental study on flat-wall-impinging spray of microhole nozzles under ultra-high injection pressures," Proceedings of the Institution of Mechanical Engineers, Part D: Journal of Automobile Engineering 222:1731–1741, 2008, doi: 10.1243/09544070JAUTO858.

[6] Glauert, M. B., "The wall jet," Journal of Fluid Mechanics 1(06):625, 1956, doi: 10.1017/S002211205600041X.

[7] Wang, X., Huang, Z., Zhang, W., et al., "Effects of ultra-high injection pressure and micro-hole nozzle on flame structure and soot formation of impinging diesel spray," Applied Energy 88(5):1620–1628, 2011, doi: 10.1016/j.apenergy.2010.11.035.

[8] Zhang, Y. and Nishida, K., "Vapor/Liquid Behaviors in Split-Injection D.I. Diesel Sprays in a 2-D Model Combustion Chamber," SAE Technical Paper, (May 2003), doi: 10.4271/2003-01-1837.

[9] Eismark, J., "On Soot Oxidation in Heavy Duty Diesel Engines," Ph.D. Chalmers University of Technology, 2012.

[10] Naber, J. D. and Siebers, D. L., "Effect of gas density and vaporization on penetration and dispersion of Diesel sprays," SAE Technical Paper 105(412):82–111, 1996, doi: 10.4271/960034.

[11] Bruneaux, G., Causse, M., and Omrane, A., "Air Entrainment in Diesel-Like Gas Jet by Simultaneous Flow Velocity and Fuel Concentration Measurements, Comparison of Free and Wall Impinging Jet Configurations," SAE International Journal of Engines 5(2):2011–01–1828, 2011, doi: 10.4271/2011-01-1828.

[12] Abani, N. and Ghandhi, J. B., "Behavior of Unsteady Turbulent Starting Round Jets," Journal of Fluids Engineering 134(6):061202, 2012, doi: 10.1115/1.4006385.

[13] Borz, M. J., Kim, Y., and O'Connor, J., "The Effects of Injection Timing and Duration on Jet Penetration and Mixing in Multiple-Injection Schedules," SAE Technical Paper, (Apr. 2016), doi: 10.4271/2016-01-0856.

[14] Eismark, J., Hammas, M., Karlsson, A., et al., "Role of turbulence for mixing and soot oxidation for an equivalent diesel gas jet during wall interaction studied with LES.," THIESEL 2012 Conference on Thermo- and Fluid Dynamic Processes in Direct Injection Engines, (2012):1–16.

[15] Poreh, M., Tsuei, Y. G., and Cermak, J. E., "Investigation of a Turbulent Radial Wall Jet," Journal of Applied Mechanics 34(2):457, 1967, doi: 10.1115/1.3607705.

[16] Knowles, K. and Myszko, M., "Turbulence measurements in radial wall-jets," Experimental Thermal and Fluid Science 17(1-2):71–78, 1998, doi: 10.1016/S0894-1777(97)10051-6.

[17] Musculus, M. P. and Kattke, K., "Entrainment Waves in Diesel Jets," SAE International Journal of Engines 2(1):1170–1193, 2009, doi: 10.4271/2009-01-1355.

[18] Pastor, J. V., Javier López, J., García, J. M., and Pastor, J. M., "A 1D model for the description of mixing-controlled inert diesel sprays," Fuel 87(13-14):2871–2885, 2008, doi: 10.1016/j.fuel.2008.04.017.

[19] Desantes, J. M., Pastor, J. V., García-Oliver, J. M., and Pastor, J. M., "A 1D model for the description of mixing-controlled reacting diesel sprays," Combustion and Flame 156(1):234–249, 2009, doi: 10.1016/j.combustflame.2008.10.008.

[20] Wood, G. S., Kwok, K. C. S., Motteram, N. A., and Fletcher, D. F., "Physical and numerical modelling of thunderstorm downbursts," Journal of Wind Engineering and Industrial Aerodynamics 89(6):535–552, 2001, doi: 10.1016/S0167-6105(00)00090-8.

[21] Borz, M. J., "Gas Jet Studies for the Characterization of Advanced Engine Schedules and Bowl Design in Diesel Engines," Master's, The Pennsylvania State University, 2016.

[22] Musculus, M. P. B., Miles, P. C., and Pickett, L. M., "Conceptual models for partially premixed low-temperature diesel combustion," Progress in Energy and Combustion Science 39(2-3):246–283, 2013, doi: 10.1016/j.pecs.2012.09.001.

Acknowledgements

Appendix

A model of the injection system was developed to better understand its behavior as experiments are run. A control volume analysis of the injector was performed to the compute the transient composition and state of the mixture in the injector chamber during the injection sequence, taking into account the gas flowing in through the valves and out the nozzle. Analysis reveals that the air initially in the injector significantly affects the composition of the injected gas. To correct for this, an effective velocity is calculated and used as the boundary condition to the free spray model.

Model

A schematic of the model is shown in Figure 22. The main components of the injector block are shown.
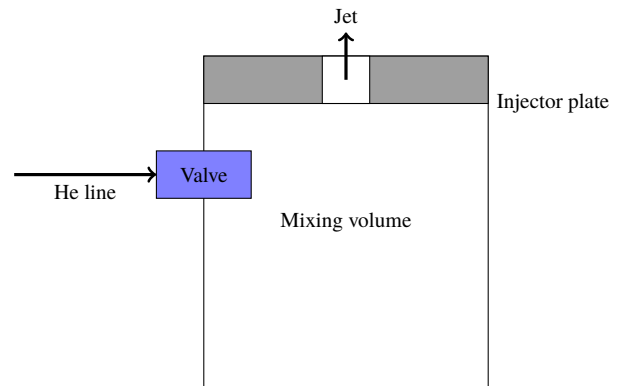

Figure 22: Schematic of the injector model.

Over each timestep simulated, the velocity of the gas entering the chamber through the solenoid valve and exiting the chamber through the nozzle is calculated assuming isentropic flow, following Abani and Ghandhi [12] and Bruneaux et. al [11]. For isentropic flow from stagnation with $P_1 > P_2$, the Mach number Ma, downstream

temperature T_2, and downstream speed of sound a_2 are calculated with

$$Ma = \sqrt{\frac{2}{\gamma - 1} \cdot \left(\frac{P_1}{P_2}\right)^{((\gamma-1)/\gamma)-1}} \tag{22}$$

$$T_2 = \frac{T_1}{1 + ((\gamma - 1)/2) \cdot Ma^2} \tag{23}$$

$$a_2 = \sqrt{\gamma R T_2} \tag{24}$$

where P_1 and T_1 are the upstream pressure and temperature, respectively (and are assumed to represent the stagnated properties), and R is the instantaneous specific gas constant for the gas in the chamber. The ratio of specific heats γ is that of the upstream fluid.

Velocity in the lines feeding the chamber and in the chamber are neglected, such that each represents stagnation conditions. However, for simplicity, the upstream temperature in both the valve flow and nozzle flow calculation is set at $T = 300$ K. This approximation is equivalent to assuming that heat is transferred through the injector walls to the gas inside sufficiently to maintain it at the ambient temperature.

The velocity and density of the jet are then calculated, respectively, with

$$u_2 = Ma \cdot a_2 \tag{25}$$

$$\rho_2 = \frac{P_2}{R T_2}. \tag{26}$$

The mass and number of moles of gas molecules passing through each point i (the valve and the nozzle) is tracked with

$$\dot{m}_i = \rho_i u_i A_{i,\text{eff}} \tag{27}$$

$$\dot{n}_i = \dot{m}_i / MM_i \tag{28}$$

where MM_i is the molar mass of the gas mixture, which changes with the chamber composition. These values are used to determine the mass and composition of the gas leaving the chamber at each point in time. The chamber volume is assumed to be 1 cm^3. The instantaneous specific gas constant for the gas in the chamber is then

$$R = \frac{R_u}{m_i / n_i} \tag{29}$$

where the universal gas constant $R_u = 8.314$ J/mol K.

Injection simulation

The input to the injector model described above is the pressure of the helium line feeding the chamber. However, the pressure transducer in the experiment measures the chamber pressure. In order to simulate the composition of the gas in the chamber during an event in which the chamber pressure follows the measured curve, the measured chamber pressure trace is used as the transient input to the model (the helium line pressure). The area of the valve connecting the helium line to the chamber is artificially increased, such that the pressure in the chamber matches that of the helium line nearly instantaneously. The measured injector pressure traces were shown in Figure 7.

Effective velocity calculation

The composition and density of the gas leaving the gas jet injector is not constant, due to air initially residing in the injector before being replaced with the fed helium. However, the spray model, which was developed for diesel sprays in which the liquid spray density is constant, assumes a constant density for the injected fluid.

A problem arises, then, when the velocity (and not the gas density) predicted by the injector model is used as the spray model's boundary conditions. With air initially in the chamber, the actual initial mass flow through the nozzle is greater than would be calculated by assuming the gas's density was that of helium, since air is more dense.

To correct for this, an "effective" nozzle velocity is calculated which serves to match the momentum flux in the simulated injection to that in the real injection and is given by

$$u_{\text{eff}} = u_{\text{isentropic}} \cdot \sqrt{\frac{\rho_{\text{isentropic}}}{\rho_{\text{assumed}}}}. \tag{30}$$

where $u_{\text{isentropic}}$ and $\rho_{\text{isentropic}}$ are calculated by the injector model and ρ_{assumed} is the assumed gas density. ρ_{assumed} is the gas density calculated with the ideal gas equation at the nominal injection pressure.

The actual (as calculated by the injector model) and effective velocities for the each of the $L = 8.2$ cm cases are plotted against time in Figure 23. The plots for the $L = 4.1$ cm cases are nearly identical, given the similarity of the pressure profiles.
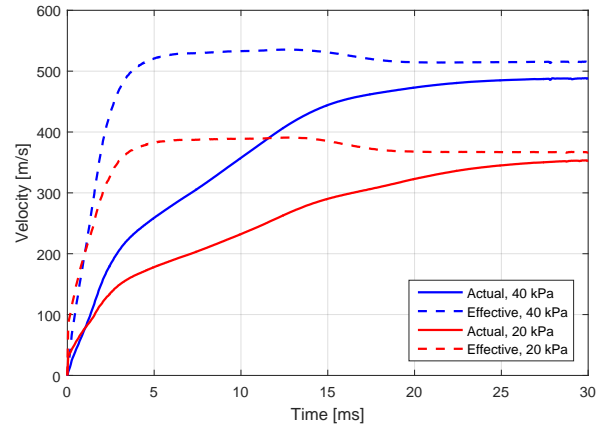

Figure 23: Actual and effective velocities for injections at 20 kPa$_g$ and 40 kPa$_g$.

The initial increase in effective velocity serves to compensate for the air that is initially in the chamber, which is at a higher density than the helium. As the air exits the chamber and the chamber becomes nearly completely helium, the effective velocity approaches the actual velocity.